Li, Y., Howcroft, C., Neild, S. A., & Jiang, J. Z. (2017). Using continuation analysis to identify shimmy-suppression devices for an aircraft main landing gear. *Journal of Sound and Vibration*, *408*, 234-251. https://doi.org/10.1016/j.jsv.2017.07.028

Using continuation analysis to identify shimmy-suppression devices for an aircraft main landing gear

Yuan Li, Chris Howcroft, Simon A. Neild, Jason Zheng Jiang*

Faculty of Engineering, University of Bristol, Bristol BS8 1TR, UK

Abstract

This paper considers several passive shimmy-suppression devices for a dual-wheel main landing gear (MLG) and proposes a method of selecting the device parameter values for which no shimmy occurs. Two of these devices include an inerter, a novel mechanical element with the property that the applied force is proportional to the relative acceleration between its terminals. A nonlinear mathematical model is developed to represent the MLG dynamics. A bifurcation study is then carried out to investigate the effects of the shimmy-suppression devices on the gear steady-state response. The aircraft forward speed and the device damping are chosen as the continuation parameters. A range of device parameter values that ensure the aircraft is free from shimmy instability for any forward speed within its operating region are identified. It is shown that the use of a proposed spring-damper configuration can result in a more robust device in terms of the device damping over that of a conventional shimmy damper. Two inerter-based shimmy-suppression devices are then considered and yield further benefits on expanding the zero-shimmy regions in the two-parameter bifurcation diagrams.

Keywords: Shimmy-suppression device; Inerter; Continuation; Steady-state solution

1. Introduction

The landing gear of any civil aircraft is required to be free from excessive vibrations and any dynamic instabilities over a conservative range of operating conditions [1]. A key source of such vibrations or instabilities is the phenomenon called shimmy. In the design process, the demand for suppressing shimmy instability may impose several design constraints on the structural stiffness and geometry of landing gear [2]. However, if modifications to geometry, stiffness or weight are infeasible or undesirable, a shimmy damper is often introduced to alter the response [3]. Normally passive dampers are used to suppress shimmy oscillations. However alternatives are available. For example, it has been proposed that that the control orifice, present in some nose-gear hydraulic steering actuators, can be used to suppress shimmy [4]. Typically the shimmy damper is modelled as a damping coefficient in parallel with the gear torsional stiffness [5]. Recently, studies have proposed semi-active or active shimmy-suppression strategies, such as using fuzzy adaptive control [6], magnetorheological damping [7], and sliding mode control [8]. However, while such semi-active

*Corresponding author
Email address: z.jiang@bristol.ac.uk (Jason Zheng Jiang)

or active controllers outperform passive ones, passive devices do have some advantages. They are typically simpler, requiring no power source, and are unconditionally stable. For example, under some circumstance when the electrical power is lost, the powered active damping systems may fail to function. So current shimmy-suppression methods are typically still passive shimmy dampers [8].

Concentrating on passive solutions, studies have been reported in which the performance of various passive devices have been assessed in conjunction with linear gear model, see for example [1, 9, 10]. In this paper, a method of selecting the network layout and parameter regions for shimmy-suppression devices is proposed. This method ensures no sustained shimmy oscillations will occur over the aircraft operating velocity range. This approach is different from previous design methods in the literature and is applicable to different mechanical structures, for example, the lag damper for helicopters.

Firstly a passive device consisting of a linear spring and damper in parallel (which we term the *shimmy damper*) is considered. The response of a dual-wheel MLG equipped with this shimmy damper is assessed. Then we investigate the effects of a proposed layout which adds a linear spring in series with the shimmy damper. In addition, configurations which include an inerter will be considered. The inerter is a commercially-available component, first proposed by Smith [11], that generates a reaction force proportional to the relative acceleration between its two terminals. It completes the analogy between mechanical and electrical systems, allowing a wide range of passive absorber structures to be realised by mechanical networks. Performance advantages of suppression devices that include inertance have been identified for various systems, including vehicle suspensions [12, 13], motorcycle steering systems [14], building vibration-suppression systems [15, 16] and railway suspensions [17, 18]. The effects of the inerter on landing gear shimmy behaviour have been reported in [19, 20], with [20] discussing the advantages of inerter-based shimmy-suppression configurations in terms of landing gear transient response.

The MLG steady-state response will be analysed using a nonlinear low-order model in this work. Here the tyre will be modelled using the exact stretched-string formulation [21], an extension of the model proposed by Von Schlippe and Dietrich in [22]. For the representation of the landing gear structure, the torsional motion is a vital consideration in capturing the shimmy mechanism, see [23] for example. Since real landing gear systems exhibit various nonlinearities, the nonlinear dynamics of landing gear have attracted significant research interest. One approach to studying the gear's nonlinear response is to use a bifurcation analysis [24]. In [25, 26], Thota et al. performed a bifurcation study to investigate the effects of the geometric nonlinearity raised by a non-zero rake angle. They found that a lateral bending motion becomes coupled with the torsional motion. Further examples of bifurcation analysis applied in nonlinear systems can be found in [27–30] where [28–30] focused on aircraft shimmy analysis in particular. Other analytical analyses have been conducted in the literature to investigate the nonlinear aircraft shimmy problem, based on the techniques of perturbation analysis [31] and the incremental harmonic balance method [32].

In this paper, we investigate the influences of the passive shimmy-suppression devices on the MLG steady-state response via continuation analysis. In Section 2, a nonlinear mathematical model of a typical MLG configuration reported in [28] is discussed. In Section 3, a passive device consisting of a linear spring and damper in parallel (the shimmy damper) is considered. A bifurcation study is carried out using the continuation software AUTO [33], which is integrated into a Matlab environment via the Dynamical Systems Toolbox [34]. This allows us to identify the device parameter region in which no sustained shimmy oscillations occur over the entire operating speed range. This region in parameter space will be defined as the *zero-shimmy region*. A beneficial

shimmy-suppression device with spring-damper layout is introduced, and its ability in expanding the zero-shimmy region are assessed. Based on this layout, two inerter-combined devices are proposed in Section 4. Their effects on the bifurcation diagrams are then studied and the performance advantages discussed. Finally, in Section 5 we draw some conclusions.

2. Main landing gear shimmy model

In this section, a typical dual-wheel MLG system reported in [28] is considered and the formulation of a low-order mathematical model of the MLG is presented. The MLG motion is modelled in terms of two degrees of freedom (DOFs); the gear torsional rotation and the lateral bending. The dynamics of the shimmy-suppression device and elastic tyres are also considered.

2.1. Dynamics of a MLG system

A sketch of the dual-wheel MLG is shown in Fig. 1 from different views. A global frame OXYZ is used here, which is fixed to the ground. The X axis points in the aircraft direction of travel, the Z axis vertically downwards, and the Y axis completes the right-handed coordinate system. The MLG consists of a main strut, side-stay, torque links, axle assembly connected with two wheels, etc. The top of the MLG is attached to the aircraft fuselage at the point A. We consider a typical orientation of the side-stay here, which is mounted laterally with respect to the main strut and is attached to the fuselage at the point F, as illustrated in Fig. 1(a). The main strut which is inclined to the Z axis by a non-zero rake angle ϕ is constructed of two cylinders or tubes. To keep the alignment of the wheels, a pair of torque links is employed, with the upper link attached to the upper strut cylinder and the lower one to the lower cylinder (piston), see Fig. 1(b). The end point of the piston is labelled C and the wheel axle is offset from the point C via a caster of length e.

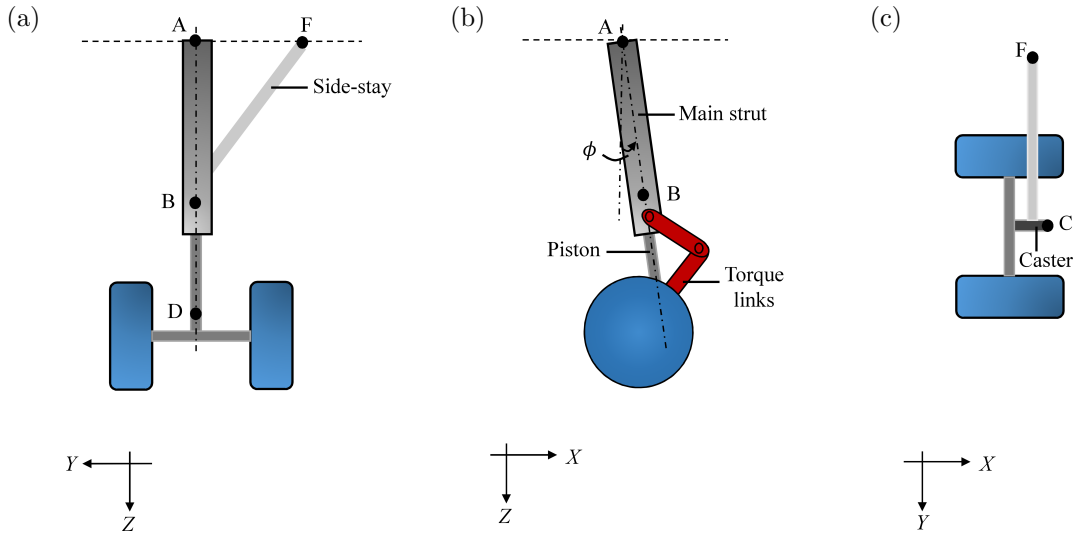

Figure 1: The dual-wheel MLG geometry.

As can be seen from Fig. 2(a), a body frame B$\xi\eta\zeta$ is used in order to describe the dynamics of the MLG system in the disturbed state. The axis ζ is rotated from the Z axis along the Y axis by

the rake angle ϕ, and is aligned with the strut axis. The axis ξ is parallel with the caster while the axis η completes the right-handed coordinate system. With a radius l_δ, the lower gear is allowed to bend laterally about point B along the ξ axis by the angle δ to represent the lateral compliance of the gear. We consider k_δ and c_δ to capture the structural stiffness and damping of such lateral motion. The gear below point B has a center of gravity located at the point D. The wheel and axle assembly may rotate about the ζ axis with the torsion angle ψ, as shown in Fig. 2(b). This represents the rotational compliance of the torque links that span the upper and lower parts of the strut and are present to provide a rotational stiffness k_ψ. A torsional damping c_ψ is also introduced to capture the MLG rotational damping. The MLG is allowed to move vertically and the vertical displacement of point B is z_B. A constraint that the tyres must always contact the ground is assumed. Note that as in [28] we do not consider any axial deflection here. Hence, δ and ψ are the two MLG DOFs. Further, we consider a shimmy-suppression device fitted in the apex location between the upper and lower torque links, as shown in Fig. 2(a). Note that the conventional shimmy damper is a translational device which generates force to control the relative movement of the two torque links. Such characteristics of the shimmy damper can be converted into equivalent torsional characteristics about the strut center line. All the following shimmy-suppression devices discussed have equivalent torsional properties. The DOF 'ε' across the device is introduced to represent the equivalent torsional motion of the shimmy-suppression device. The overall equivalent torque T_ψ generated by torsional damping, torque link stiffnesses and shimmy-suppression device is illustrated in Fig. 2(b). As presented in [1, 9, 20], the torsional stiffness k_ψ is treated as a series connection between the suppression device and the MLG torsional motion. Such MLG torsional mechanism is illustrated in Fig. 3(a).

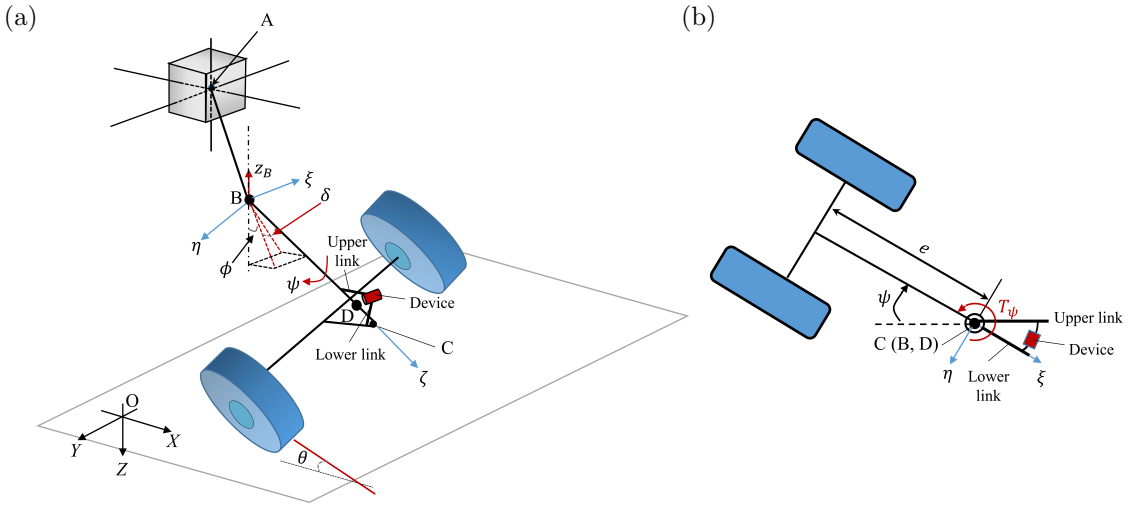

Figure 2: Schematic of (a) the MLG system in the disturbed state and the location of shimmy-suppression device, (b) the ψ degree of freedom in the C$\xi\eta$ plane. The toque T_ψ represents the overall equivalent torque generated by torsional damping, torque link stiffness and shimmy-suppression device.

In this work the MLG mathematical model is established using the Lagrangian method. For

each DOF, Lagrange's equation holds,

$$\frac{\partial}{\partial t}\left(\frac{\partial L}{\partial \dot{q}_i}\right) - \frac{\partial L}{\partial q_i} + \frac{\partial D}{\partial \dot{q}_i} = Q_i, \tag{1}$$

where L is Lagrangian and $L = T - U$, T and U represent the kinetic and potential energy of the MLG system, respectively. D is Rayleigh's dissipative function, Q_i is the generalised force applied to the MLG system and q_i is the generalised coordinate. When deriving the equations of motion for the system, z_B is temporarily treated as a MLG DOF before being eliminated using a compatibility equation of the tyre-ground contact constraint.

The MLG kinetic energy is

$$T = \frac{1}{2}(m_D|\mathbf{v_D}|^2 + \boldsymbol{\omega_\delta}^T \boldsymbol{J_D} \boldsymbol{\omega_\delta} + \boldsymbol{\omega_\psi}^T \boldsymbol{J_D} \boldsymbol{\omega_\psi}), \tag{2}$$

where m_D is the mass of the lower gear (below B), $\boldsymbol{J_D}$ is the inertia matrix at point D in the global frame, $\mathbf{v_D}$ is the velocity vector of the point D, $\boldsymbol{\omega_\delta}$ and $\boldsymbol{\omega_\psi}$ are the angular velocity vectors of the points D (lateral bending motion) and C (torsional motion), respectively. The potential energy is

$$U = \frac{1}{2}(k_\delta \delta^2 + k_\psi(\psi - \varepsilon)^2). \tag{3}$$

The ε DOF, representing the motion across the shimmy-suppression device, can be eliminated using a compatibility equation. The torque generated by the shimmy-suppression device T_d is balanced by the torsional spring torque $k_\psi(\psi - \varepsilon)$, as illustrated in Fig. 3(a). The expression for T_d is dependent on the device layout. For the shimmy damper layout (labelled L1) shown in Fig. 3(b), the compatibility equation is given by

$$T_d = k_d\varepsilon + c_d\dot{\varepsilon} = k_\psi(\psi - \varepsilon), \tag{4}$$

where k_d and c_d denote the stiffness and damping of the device. It should be noted that k_d is included and fixed at a default value for all the shimmy-suppression device layouts considered. This is to ensure the gear has sufficient rotational stiffness for centering the gear. The default value of k_d was determined via a scaling calculation based on [9], which is 1.09×10^5 Nm/rad. The Rayleigh's dissipative function is given by

$$D = \frac{1}{2}(c_\delta \dot{\delta}^2 + c_\psi \dot{\psi}^2), \tag{5}$$

where c_δ and c_ψ are the damping coefficients of the respective DOF.

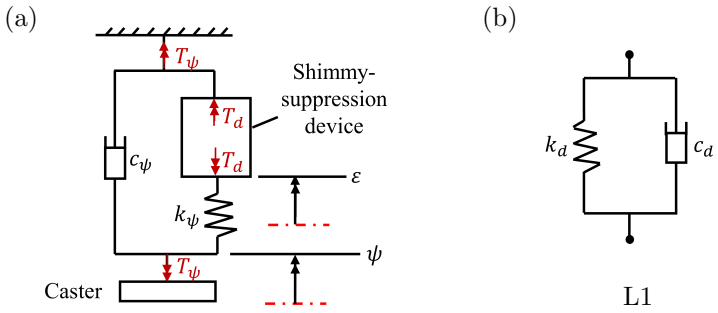

Figure 3: View of (a) the MLG torsional mechanism, (b) the layout of the default shimmy damper.

Now we need to determine the exact expression of T based on Eq. (2). We consider all the terms in the global frame, so it is desirable to define the rotation matrix transforming the vectors from the body frame to the global one. As the global frame can be transformed to the body frame via three rotations ϕ-δ-ψ in sequence, this matrix is given by

$$\boldsymbol{H} = \begin{bmatrix} \cos\phi\cos\psi + \sin\phi\sin\delta\sin\psi & -\cos\phi\sin\psi + \sin\phi\sin\delta\cos\psi & \sin\phi\cos\delta \\ \cos\delta\sin\psi & \cos\delta\cos\psi & -\sin\delta \\ -\sin\phi\cos\psi + \cos\phi\sin\delta\sin\psi & \sin\phi\sin\psi + \cos\phi\sin\delta\cos\psi & \cos\phi\cos\delta \end{bmatrix}. \tag{6}$$

The position and velocity vectors of point B in the global frame are given by

$$\boldsymbol{r_B^G} = \begin{bmatrix} Vt \\ 0 \\ -(z_B + L_A - l_B\cos\phi) \end{bmatrix}, \ \boldsymbol{v_B} = \dot{\boldsymbol{r}}_{\boldsymbol{B}}^{\boldsymbol{G}} = \begin{bmatrix} V \\ 0 \\ -\dot{z}_B \end{bmatrix}, \tag{7}$$

where V is the aircraft forward speed, t is the time, L_A is the MLG height, and l_B is the distance from points A to B. The position vector of point D in the body frame is given by

$$\boldsymbol{r_{BD}^b} = \begin{bmatrix} 0 \\ 0 \\ l_D \end{bmatrix}, \tag{8}$$

where l_D is the distance from B to D. Then, we obtain the position and velocity vectors of point D in the global frame by

$$\boldsymbol{r_D^G} = \boldsymbol{r_B^G} + \boldsymbol{H}\boldsymbol{r_{BD}^b}, \quad \boldsymbol{v_D} = \dot{\boldsymbol{r}}_{\boldsymbol{D}}^{\boldsymbol{G}}. \tag{9}$$

Due to the sequenced rotations applied from global to body frames, the two angular velocity vectors may be written as

$$\boldsymbol{\omega_\delta} = \begin{bmatrix} \dot{\delta}\cos\phi \\ 0 \\ -\dot{\delta}\sin\phi \end{bmatrix}, \ \boldsymbol{\omega_\psi} = \begin{bmatrix} \dot{\psi}\cos\delta\sin\phi \\ -\dot{\psi}\sin\delta \\ -\dot{\psi}\cos\phi\cos\delta \end{bmatrix}. \tag{10}$$

The inertia matrix tensor is given by

$$\boldsymbol{J_D^b} = \begin{bmatrix} J_{D\xi\xi}^b & 0 & 0 \\ 0 & J_{D\eta\eta}^b & 0 \\ 0 & 0 & J_{D\zeta\zeta}^b \end{bmatrix}, \tag{11}$$

where J_{DWW}^b represents the moment of inertia at point D with respect to W axis of the body frame. Hence, the inertia matrix tensor in the global frame can be given by

$$\boldsymbol{J_D^G} = \boldsymbol{H}\boldsymbol{J_D^b}\boldsymbol{H}^T. \tag{12}$$

Fig. 4 shows the external forces applied to the MLG system. There is a vertical force F_N acting on the point B and the gravitational force at point D, giving

$$\boldsymbol{F_B} = \begin{bmatrix} 0 \\ 0 \\ F_N \end{bmatrix}, \ \boldsymbol{G_D} = \begin{bmatrix} 0 \\ 0 \\ m_D g \end{bmatrix}, \tag{13}$$

where $F_N = Mg$, M is the mass of the fuselage and the upper part of the MLG (that above point B), and g is the gravitational constant. At the ground-tyre contact points, there are vertical forces $\boldsymbol{F_{zi}}$ and lateral forces $\boldsymbol{F_{yi}}$, where $i = L$ or R represents the force applied to the left or right tyre. These are given by

$$\boldsymbol{F_{zi}} = \begin{bmatrix} 0 \\ 0 \\ -F_{zi} \end{bmatrix}, \ \boldsymbol{F_{yi}} = \begin{bmatrix} -F_{zi}\Lambda_i \sin\theta \\ F_{zi}\Lambda_i \cos\theta \\ 0 \end{bmatrix}, \tag{14}$$

where F_{zi} is the magnitude of $\boldsymbol{F_{zi}}$, $\theta = \psi \cos\phi \cos\delta$ is the angle between the wheel actual travelling direction and the X axis. The expression of the coefficient Λ_i is dependent on the tyre model and will be given in Section 2.2. The vertical forces are given by

$$F_{zL} = \frac{1}{2}(-a\mu k_t + F_z), \quad F_{zR} = \frac{1}{2}(a\mu k_t + F_z), \tag{15}$$

where k_t is the tyre vertical stiffness, F_z is the total vertical force acting on the MLG from the ground, and a is the track width, as illustrated in Fig. 4. The angle μ is given by

$$\mu = \sin^{-1}(\sin\phi \sin\psi + \cos\phi \sin\delta \cos\psi). \tag{16}$$

Apart from the forces, the tyres also experience self-aligning moments $\boldsymbol{M_{ki}}$, as given by

$$\boldsymbol{M_{ki}} = \begin{bmatrix} 0 \\ 0 \\ -C_{ki}F_{zi} \end{bmatrix}, \tag{17}$$

where C_{ki} will be given in Section 2.2. The velocity vectors at ground-tyre contact points E_i are also needed for the calculation of the generalised forces. The positions of E_i in the body frame are given by

$$\boldsymbol{r^b_{BEi}} = \begin{bmatrix} -(e + R_i \sin\phi) \\ \mp\frac{a}{2} \\ l_\delta + R_i \cos\phi \end{bmatrix}, \tag{18}$$

where R_i is loaded radius of the left/right tyre. R_i can be expressed by

$$R_i = R - 0.2d_i, \tag{19}$$

where R is the tyre unloaded radius, $d_i = \mp\frac{1}{2}a\mu$, which represents the tyre deflections (see Daugherty [35]). Then, the position and velocity vectors can be calculated by

$$\boldsymbol{r^G_{Ei}} = \boldsymbol{r^G_{Bi}} + \boldsymbol{H r^b_{BEi}}, \quad \boldsymbol{v_{Ei}} = \boldsymbol{\dot{r}^G_{Ei}}. \tag{20}$$

Thus, the generalised force for each coordinate is calculated by

$$Q_i = \boldsymbol{F_B} \cdot \frac{\partial \boldsymbol{v_B}}{\partial \dot{q}_i} + \boldsymbol{G_D} \cdot \frac{\partial \boldsymbol{v_D}}{\partial \dot{q}_i} + \sum_{i=L,R} (\boldsymbol{F_{yi}} + \boldsymbol{F_{zi}}) \cdot \frac{\partial \boldsymbol{v_{Ei}}}{\partial \dot{q}_i} + \sum_{i=L,R} \boldsymbol{M_{ki}} \cdot \frac{\partial(\boldsymbol{\omega_\delta} + \boldsymbol{\omega_\psi})}{\dot{q}_i}. \tag{21}$$

This completes the set of terms needed for Eq. (1).

As previously mentioned, the ground-contact constraint ensures the MLG always contacts the ground. Therefore, the velocities of the contact points in the vertical direction should equal 0, giving

$$v_{Ei.Z} = \dot{z}_B - \dot{r}_{BEi.Z} = 0, \tag{22}$$

where $v_{Ei.Z}$ and $\dot{r}_{BEi.Z}$ are the Z components of $\boldsymbol{v_{Ei}}$ and $\dot{\boldsymbol{r}}^{\boldsymbol{G}}_{\boldsymbol{BEi}}$ ($\boldsymbol{r}^{\boldsymbol{G}}_{\boldsymbol{BEi}} = \boldsymbol{H}\boldsymbol{r}^{\boldsymbol{b}}_{\boldsymbol{BEi}}$), respectively. Therefore, to satisfy this constraint for the two contact points, we have

$$\dot{z}_{BL} = \dot{r}_{BEL.Z}, \tag{23}$$

$$\dot{z}_{BR} = \dot{r}_{BER.Z}. \tag{24}$$

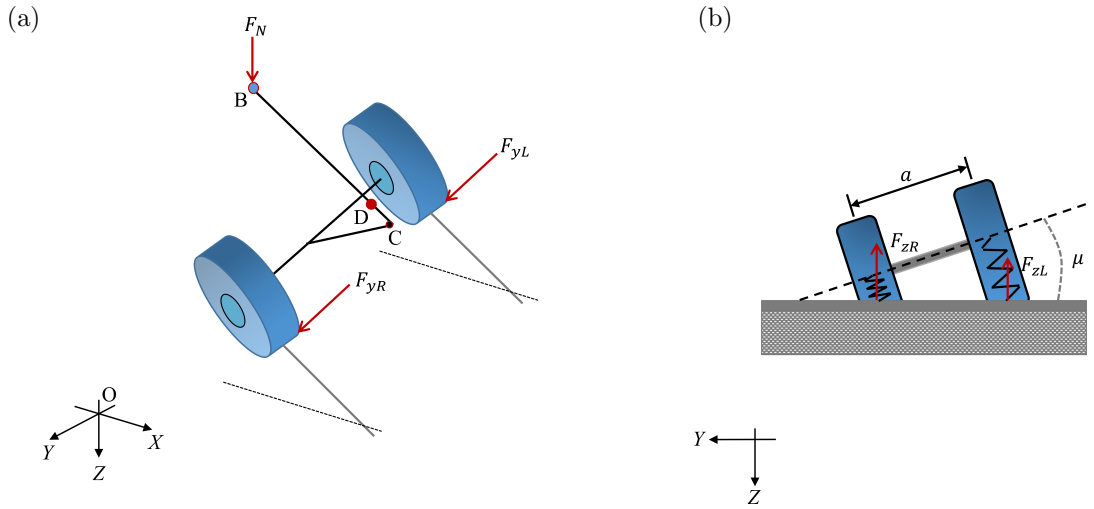

Figure 4: View of (a) the general forces applied to the MLG, (b) the vertical forces acting at the ground contact points of the two wheels.

2.2. Tyre model

The exact stretched-string model detailed in [21] is used here to capture the tyre dynamics, and will be discussed in two parts. The first part involves the forces applied to the MLG, i.e., the lateral forces $\boldsymbol{F_{yi}}$ and the self-aligning moments $\boldsymbol{M_{ki}}$. According to the tyre model, to capture these forces, the definitions of coefficients Λ_i and C_{ki} need to be provided, written as

$$\Lambda_i = k_\lambda \tan^{-1}(7 \tan \alpha_i \cos(0.95 \tan^{-1}(7 \tan \alpha_i))), \tag{25}$$

and

$$C_{ki} = \begin{cases} k_\alpha \frac{\alpha_m}{\pi} \sin(\alpha_i \frac{\pi}{\alpha_m}) & \text{if } |\alpha_i| \leq \alpha_m \\ 0 & \text{if } |\alpha_i| > \alpha_m \end{cases}, \tag{26}$$

where k_λ is the tyre restoring coefficient, $\alpha_i = \tan^{-1}(\frac{\lambda_i}{l})$ is the tyre slip angle and l is the tyre relaxation length. In Eq. (26), k_α is the tyre self-aligning coefficient and α_m is the maximum slip angle. These definitions are taken from [26].

The second part relates to the tyre dynamics at the ground-tyre contact plane. As shown in Fig. 5, the local tyre frame $\mathrm{E}_i xy$ is used and the actual shape of the tyre contact line is defined by a function $\mathrm{P}_i(x,t)$, $x \in [-h, h]$, where $2h$ is the contact patch length. Consider a point P_i between the leading and trailing points (P_1 and P_2, respectively) of the contact patch, it has a

lateral deformation $y_i(x,t)$ along y axis. Then the absolute position of the point P_i is given by

$$\boldsymbol{r}_{\boldsymbol{Pi}}^{\boldsymbol{G}} = \boldsymbol{r}_{\boldsymbol{Ei}}^{\boldsymbol{G}} + \boldsymbol{r}_{\boldsymbol{EPi}}^{\boldsymbol{G}} = \begin{bmatrix} r_{Ei.X} + x\cos\theta - y_i(x,t)\sin\theta \\ r_{Ei.Y} + x\sin\theta + y_i(x,t)\cos\theta \\ r_{Ei.Z} \end{bmatrix}, \tag{27}$$

where $r_{Ei.X}$, $r_{Ei.Y}$ and $r_{Ei.Z}$ denote the X, Y and Z components of the vector $\boldsymbol{r}_{\boldsymbol{Ei}}^{\boldsymbol{G}}$. Then its velocity vector is given by

$$\boldsymbol{v}_{\boldsymbol{Pi}} = \dot{\boldsymbol{r}}_{\boldsymbol{Pi}}^{\boldsymbol{G}} = \begin{bmatrix} v_{Ei.X} + \dot{x}\cos\theta - \dot{\theta}x\sin\theta - \dot{\theta}y_i\cos\theta - (\dot{y}_i + \frac{\partial y_i}{\partial x}\dot{x})\sin\theta \\ v_{Ei.Y} + \dot{x}\sin\theta + \dot{\theta}x\cos\theta - \dot{\theta}y_i\sin\theta + (\dot{y}_i + \frac{\partial y_i}{\partial x}\dot{x})\cos\theta \\ v_{Ei.Z} \end{bmatrix}, \tag{28}$$

where $v_{Ei.X}$, $v_{Ei.Y}$ and $v_{Ei.Z}$ denote the X, Y and Z components of the vector $\boldsymbol{v}_{\boldsymbol{Ei}}^{\boldsymbol{G}}$.

Assuming the tyres are fully adhered to the ground leads to a zero velocity condition at the point P_i, whereby each component of the vector $\boldsymbol{v}_{\boldsymbol{pi}}$ equals 0. Further algebraic manipulation gives

$$\dot{y}_i = v_{Ei.X}\sin\theta - v_{Ei.Y}\cos\theta - x\dot{\theta} - \frac{\partial y_i}{\partial x}(\dot{\theta}y_i - v_{Ei.X}\cos\theta - v_{Ei.Y}\sin\theta). \tag{29}$$

The slope at P_{1i} is related to the lateral deformation of the leading point λ_i by the approximation

$$\frac{\partial y_i(h,t)}{\partial x} = -\frac{\lambda_i}{l}. \tag{30}$$

Substitution of Eq. (30) into Eq. (29) gives

$$\dot{\lambda}_i = v_{Ei.X}(\sin\theta - \frac{\lambda_i}{l}\cos\theta) - v_{Ei.Y}(\cos\theta + \frac{\lambda_i}{l}\sin\theta) - (h - \frac{\lambda_i^2}{l})\dot{\theta}. \tag{31}$$

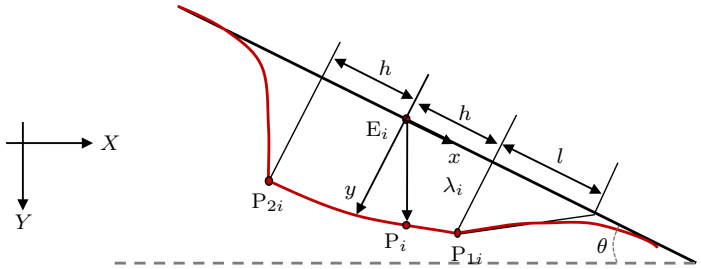

Figure 5: The stretched-string tyre model and the tyre deformation λ_i.

2.3. Equations of motion

The equations of motion of the MLG system for $q_i = \delta, \psi$ and z_B are now written in the compact form

$$N_{11}^{\delta}\ddot{\delta} + N_{12}^{\delta}\ddot{z}_B + N_{21}^{\delta}\dot{\delta}^2 + N_{22}^{\delta}\dot{\delta}\dot{\psi} + N_3^{\delta}\dot{\delta} + N_4^{\delta}\delta + N_{5L}^{\delta}F_{zL} + N_{5R}^{\delta}F_{zR} + N_6^{\delta} = 0, \tag{32}$$

$$N_1^{\psi}\ddot{\psi} + N_{21}^{\psi}\dot{\delta}^2 + N_3^{\psi}\dot{\psi} + T_d + N_{5L}^{\psi}F_{zL} + N_{5R}^{\psi}F_{zR} = 0, \tag{33}$$

$$N_{11}^{z}\ddot{z}_B + N_{12}^{z}\ddot{\delta} + N_{21}^{z}\dot{\delta}^2 - F_{zL} - F_{zR} + m_D g + F_N = 0. \tag{34}$$

Via necessary substitutions, we obtain

$$F_{zL} = \frac{1}{2}(-a\mu k_t + N^z_{11}\ddot{z}_{BL} + N^z_{21}\dot{\delta}^2 + m_D g + F_N), \tag{35}$$

$$F_{zR} = \frac{1}{2}(a\mu k_t + N^z_{11}\ddot{z}_{BR} + N^z_{21}\dot{\delta}^2 + m_D g + F_N), \tag{36}$$

where $\ddot{z}_{Bi}$ is obtained via differentiation of the two constraints Eqs. (23) and (24). The expression of the shimmy-suppression dynamics, given by Eq. (4), is specific to the type of the device considered. Hence, the three second-order differential equations Eqs. (32)–(34), the first order differential equation Eq. (31) for tyres, along with Eq. (4), complete the equations of motion for the MLG system. The coefficients N^b_{aa} are detailed in the Appendix. The parameter values shown in Table 1 are used for the MLG system and are mostly taken from [28]. The stiffness for the shimmy-suppression device, k_d, is calculated via the scaling analysis based on [9]. Note that all the parameters in Table 1 are fixed in the following discussions.

Table 1: Parameters values used in the analysis

Symbol	Parameter	Value
	MLG parameter	
a	Track width	0.5 m
c_δ	Lateral damping of the strut	300 Nms/rad
c_ψ	Torsional damping of the wheel assembly	300 Nms/rad
e	Caster length	0.12 m
k_δ	Lateral stiffness of the strut	6.1×10^6 Nm/rad
k_ψ	Effective torsional stiffness of the torque links	3.8×10^5 Nm/rad
$J^b_{D\xi\xi}$	Moment of inertia at D with respect to ξ axis	200 kgm^2
$J^b_{D\eta\eta}$	Moment of inertia at D with respect to η axis	250 kgm^2
$J^b_{D\zeta\zeta}$	Moment of inertia at D with respect to ζ axis	100 kgm^2
l_D	Distance from B to D	0.72 m
l_δ	Radius of lateral bending motion	0.75 m
m_D	Mass of the MLG bending part	500 kg
ϕ	MLG rake angle	0.0524 rad (3°)
	Tyre parameter	
h	Half of contact patch length	0.1 m
k_t	Tyre vertical stiffness	7.0×10^5 N/m
k_α	Tyre self-aligning coefficient	1.0 m
k_λ	Tyre restoring coefficient	0.002 /rad
l	Relaxation length	0.3 m
R	Tyre unloaded radius	0.362 m
α_m	Maximum slip angle	0.1745 rad
	Shimmy-suppression device parameter	
k_d	Device stiffness	1.09×10^5 Nm/rad
	Other	
g	Gravitational constant	9.81 m/s^2
M	Mass of the fuselage and the upper MLG	19.9 t

3. Analysis of non-inerter shimmy-suppression devices

Using the model presented in Section 2, two shimmy-suppression devices are investigated in this section, the first of which is the traditional shimmy-suppression device, the shimmy damper, shown in Fig. 3(b). Its effects on the MLG steady-state response are studied via continuation. The continuation approach allows the region in parameter space in which no steady-state shimmy oscillation solutions exist at any velocity within the operating range, the zero-shimmy region, to be identified. This is achieved via two-parameter bifurcation analysis in terms of forward velocity V and shimmy-suppression device damping c_d. The second proposed device comprises a spring-damper layout and the influence of this configuration on expanding the zero-shimmy region is explored. This zero-shimmy region, in which no sustained oscillations exist, has previously been studied in terms of operating conditions, see for example [36, 37]. Here it is considered also in terms of device parameter values. We note that establishing such zero-shimmy parameter region is the first design stage for shimmy-suppression device. Once it has been identified that no steady-state shimmy solutions exist, the emphasis of the device design shifts to its second stage, which is to minimise the maximum transient shimmy deflections due to perturbation, see for example [8, 20]. However, it is the first phase that is the focus of the work presented here.

3.1. The default shimmy damper

In this subsection, the effects of a shimmy damper are analysed. The device stiffness k_d is fixed to 1.09×10^5 Nm/rad and the influence of the device damping c_d on the MLG steady-state dynamic behaviour is investigated. First, choosing the aircraft forward speed as the continuation parameter while setting c_d to three example values, one-parameter bifurcation diagrams are constructed showing both the MLG steady-state zero-amplitude and periodic solutions within a certain range of speeds. After that, we treat c_d as a second continuation parameter and the resulting two-parameter bifurcation diagram is given in the parameter plane of the MLG forward speed and c_d. Regions in which different types of shimmy oscillations occur as well as stable zero-shimmy behaviour are identified in this parameter space.

3.1.1. One-parameter continuation

A bifurcation study is conducted here to investigate the MLG steay-state solutions; see [38] as an example for details of bifurcation theory and [39] as a review of applications of bifurcation analysis for aircraft dynamics. The continuation software AUTO [33], which has been integrated into Matlab via the Dynamical Systems Toolbox [34], is used in the analysis.

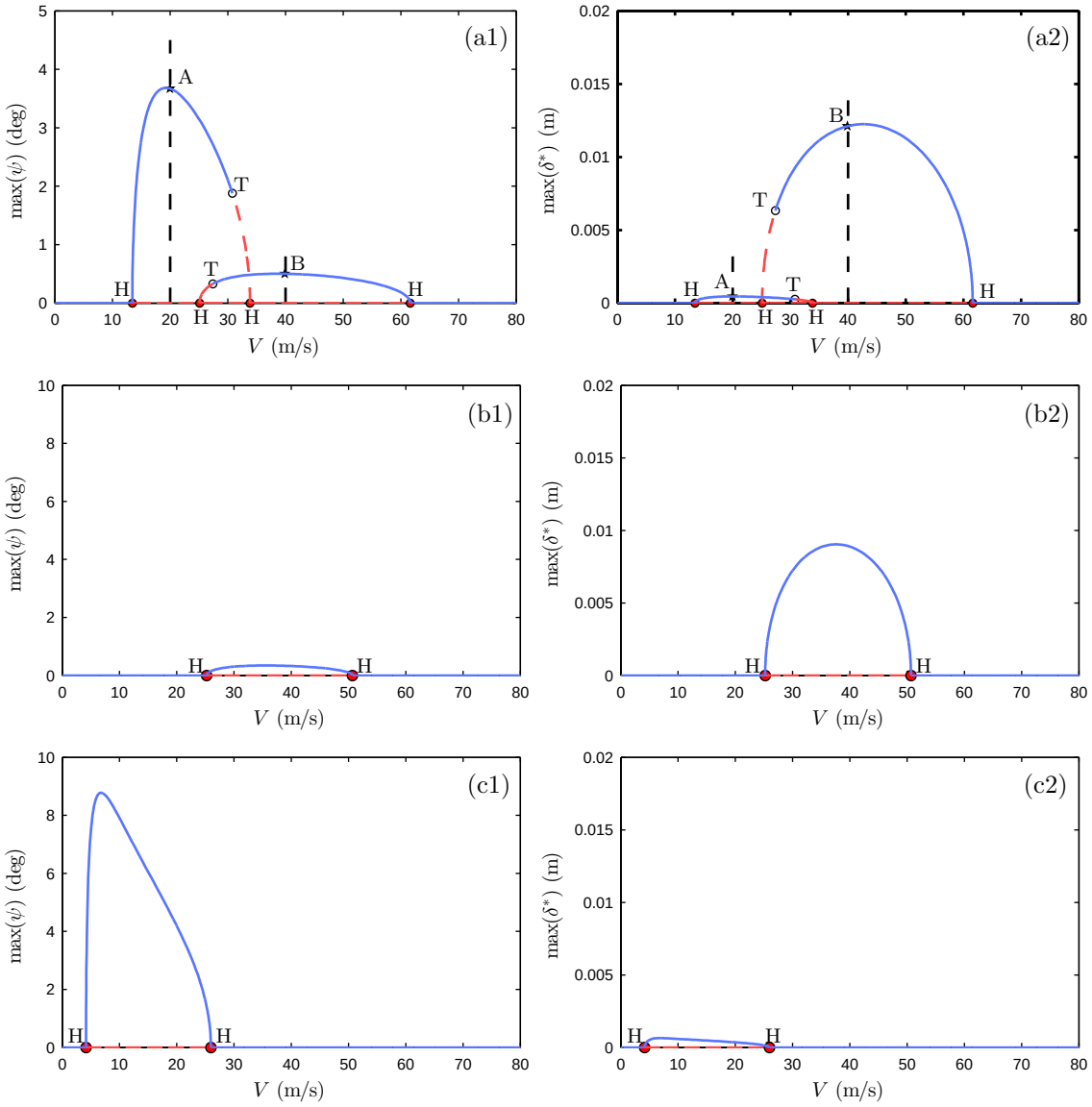

Figure 6: One-parameter bifurcation diagrams in V. Panels (a1) and (a2) are for the damping $c_d = 3.6\times10^4$ Nms/rad; (b1) and (b2) for the damping $c_d = 5.0 \times 10^3$ Nms/rad; (c1) and (c2) for $c_d = 2.0 \times 10^3$ Nms/rad. Shown are the maxima of the torsional angle ψ (left column) and of deflections δ^* (right column). Stable solutions are represented by blue solid lines and unstable solutions by red dashed lines; Hopf bifurcation points (H) are shown as red dots, and torus bifurcation points (T) as no-fill circles. The star points A and B in (a1) and (a2) correspond to the cases in which $V = 20$ and 40 m/s, respectively.

A one-parameter bifurcation analysis is now performed with the aircraft forward speed V as the continuation parameter. Fig. 6(a) shows with respect to V the maximum amplitudes of MLG

steady-state solutions in terms of torsional motion ψ and lateral bending motion δ^* when $c_d = 3.6 \times 10^4$ Nms/rad. Here, δ^* represents the resulting deflection of δ DOF at the point C. The stable solutions are represented by blue solid lines and unstable by red dashed ones. At low forward speeds, the straight-rolling solution is observed, which represents zero shimmy. When V is 13.4 m/s, the zero-shimmy solution loses stability and shimmy occurs. This qualitative change in behaviour is due to a Hopf bifurcation (labelled H) corresponding to a pair of complex conjugate eigenvalues crossing the imaginary axis in the complex plane; this gives birth to a periodic solution. This periodic branch ends with another Hopf point at $V = 33.8$ m/s. Along this branch, stability is changed at $V = 30.8$ m/s, with the existence of a torus bifurcation point (labelled T), resulting from a pair of complex eigenvalues with unit modulus. Note that for $V = 20$ m/s (point A in Fig. 6(a)) the maximum deflection angle of ψ is 3.7 degrees while the maximum amplitude of δ^* is only of the order of 10^{-4} m. We define this solution as a kind of torsional-dominated shimmy (we refer to this as ψ-shimmy). It can be observed that along this branch the maximum deflection angle of ψ is always more significant than that of δ^*. Hence this branch represents ψ-shimmy. Moreover, there is another branch of periodic solutions which is connected by a further pair of Hopf bifurcation points. Following this branch, initially the solution is unstable but regains stability when a torus point is traversed at $V = 27.4$ m/s. Similarly, we observe that the response in this branch is dominated by the lateral bending motion, see $V = 40$ m/s (point B in Fig. 6(a)) as an example, and hence is referred to as δ-shimmy. Note that there is a velocity region bounded by the two torus bifurcations, where both branches are stable; within this bistable region the initial perturbation determines which solution branch will be observed. Fig. 6(b) and (c) shows one-parameter bifurcation diagrams for smaller device damping: (b1) and (b2) for $c_d = 5.0 \times 10^3$ Nms/rad; (c1) and (c2) for $c_d = 2.0 \times 10^3$ Nms/rad. In contrast to the results shown in Fig. 6(a), for both cases, only one branch is observed and along this branch the solutions are stable. Since the δ-component is more significant in Fig. 6(b), the branch is δ-shimmy while that shown in (c) is a ψ-shimmy branch.

3.1.2. Two-parameter continuation

As observed in Fig. 6, the device damping c_d plays a significant role in the MLG dynamic behaviour. Hence, in order to investigate the influence of the device damping c_d, we choose c_d as the second continuation parameter and construct a two-dimensional bifurcation diagram in the (V, c_d)-plane. This is illustrated in Fig. 7. Fig. 6 represents the three slices $c_d = 3.6 \times 10^4$, 5.0×10^3 and 2.0×10^3 Nms/rad in the two-dimensional plane. The red curves in Fig. 7 are Hopf curves which are formed via the continuation of the Hopf point H in the one-dimensional plane. In the (V, c_d)-plane, we observe two Hopf curves intersected with a pair of Hopf-Hopf points (labelled HH). Two curves of torus bifurcations emerge from the two HH points. The third Hopf curve is observed in the lower area of the (V, c_d)-plane. As discussed in the one-parameter bifurcation analysis, the existence of Hopf points represents the onset of shimmy oscillations. Similarly, in Fig. 7, these Hopf curves bound regions of different shimmy behaviour. In particular, we find two ψ-shimmy (left-shaded) and one δ-shimmy (right-shaded) region. Grey-shaded areas indicate (V, c_d) regions in which no shimmy solutions exist. Consequently, a region $c_d \in (2754.1, 3019.4)$ bounded by the two blue lines, see insert plot in Fig. 7, is also observed. In this region the landing gear will not have sustained shimmy oscillations at any forward speed over the operating range 0–200 m/s. Specifically, this indicates that if the damping of the shimmy damper is designed in the range (2754.1, 3019.4), the MLG will be free of shimmy for any value of V–this is the zero-shimmy region.

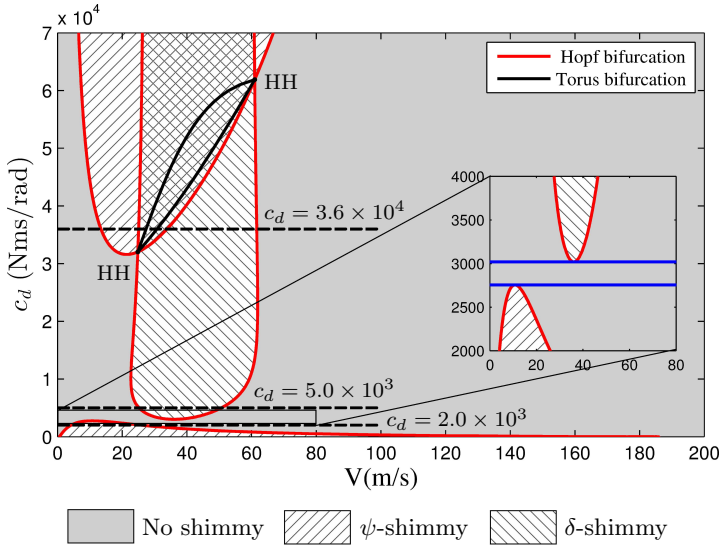

Figure 7: Two-parameter bifurcation diagrams in the (V, c_d)-plane of the MLG with the shimmy damper. The regions of no shimmy, torsional ψ-shimmy and lateral δ-shimmy are shown. The points labelled HH are double Hopf points. (For interpretation of the references to color in this figure, the reader is referred to the web version of this paper.)

3.2. A beneficial spring-damper layout

From Fig. 7, we found that if the damping of the shimmy damper is designed in the zero-shimmy region, the MLG will be free from instabilities for any forward velocity. However, this zero-shimmy region (2754.1, 3019.4) is quite narrow, so placing tight requirements for the design of the damper, such that it remains in this region for all operating conditions while also accounting for other damping contributions such as joint friction. Hence, it is desirable to expand this zero-shimmy region to provide a more flexible design requirement. To achieve this, we now investigate how varying the stiffness properties will affect the zero-shimmy region.

Note that the focus of this work is the shimmy-suppression device while the structural stiffness as listed in Table 1 will not be changed. The suppression device comprises a torsional stiffness k_s connected in series to a spring-damper pair. This configuration is denoted L2 and is depicted in Fig. 8. Panel (a) illustrates that, when equipped with the shimmy damper, k_ψ and k_s contribute to give the effective stiffness $k_{\psi e}$. These stiffnesses are related by the expression

$$k_{\psi e} = (\frac{1}{k_\psi} + \frac{1}{k_s})^{-1}. \tag{37}$$

We note that if $k_s = \infty$, $k_{\psi e}$ would equal k_ψ, otherwise $k_{\psi e} < k_\psi$. Now we can investigate the effects of varying $k_{\psi e}$ via varying k_s of L2 on the two-parameter bifurcation diagrams. Fig. 9 shows a series of continuations in the (V, c_d)-plane when varying the values of k_s. The black lines in Fig. 9(a) which represents $k_s = \infty$ case is equivalent to that in Fig. 7. Note that the torus bifurcations curves are omitted for Fig. 9 and the following two-parameter bifurcation diagrams. The dominant types of shimmy oscillations are similar to these shown in Fig. 7 and so are not marked by shading in this plot. It can be observed from Fig. 9(a) that when decreasing k_s from ∞, the δ-shimmy region

shrinks and the two ψ-shimmy regions become more significant. This indicates that a smaller k_s, and hence a smaller torsional stiffness, would stabilise the MLG δ-shimmy while destabilising the ψ-shimmy. Fig. 9(b) shows that if k_s is decreased to 5.9×10^5 Nm/rad, the δ-shimmy region disappears and a wide zero-shimmy region is found. However, if k_s is reduced further, the two ψ-shimmy regions intersect each other eliminating the zero-shimmy region.

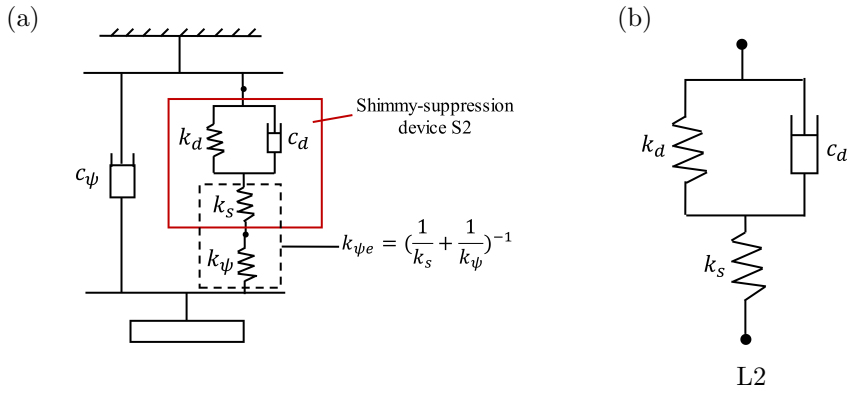

Figure 8: View of (a) the effective structural stiffness $k_{\psi e}$, (b) the proposed spring-damper device layout.

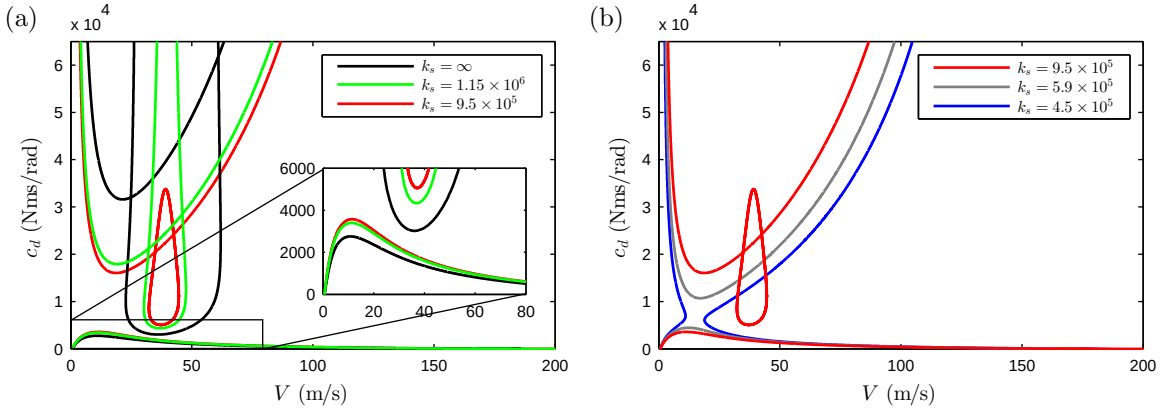

Figure 9: Two-parameter bifurcation diagrams in the (V, c_d)-plane for varying the stiffness k_s (Nm/rad) of L2. (For interpretation of the references to color in this figure, the reader is referred to the web version of this paper.)

To identify the sensitivity of the system to the variations of k_s in L2 qualitatively, four boundary points of the three shimmy regions in the (V, c_d)-plane are defined, as shown in Fig. 10(a). BP1 and BP3 are the boundary points of the upper and lower ψ-shimmy regions, respectively. BP2$_u$ and BP2$_l$ represent the upper and lower boundaries of the δ-shimmy region. As k_s is varied the c_d values of these four boundary points form four curves in Fig. 10(b), and the grey area represents the zero-shimmy region. It can be observed that the red (BP3) and blue (BP1) lines intersect at $k_s = 4.73 \times 10^5$ Nms/rad. When k_s is increased from this value, the zero-shimmy region is growing to the maximum until the green lines, i.e. the δ-shimmy region, arise at $k_s = 7.86 \times 10^5$ Nms/rad.

The grey area then splits into two parts, one is bounded by BP3 and $BP2_u$, the other by BP1 and $BP2_l$. Fig. 10(c) shows the width of the grey area with respect to the value of k_s and we define this width as the *width in damping of the zero-shimmy region*. It can be seen that the zero-shimmy region is largest in terms of damping values ($c_d \in (3813.7, 14032.7)$) at $k_s = 7.86 \times 10^5$ Nms/rad; at this point the width in damping of this region is 1.02×10^4 Nms/rad ($14032.7 - 3813.7$), which is approximately 38 times what is obtainable with the shimmy damper alone ($k_s = \infty$). After the maximum value, the width in damping of the zero-shimmy region reduces sharply, as shown by the two green lines of Fig. 10(c). Therefore, comparing with the original shimmy damper case, this beneficial spring-damper layout L2 is seen to provide a greater allowable damping range over which the MLG will be free from shimmy for all operating velocities.

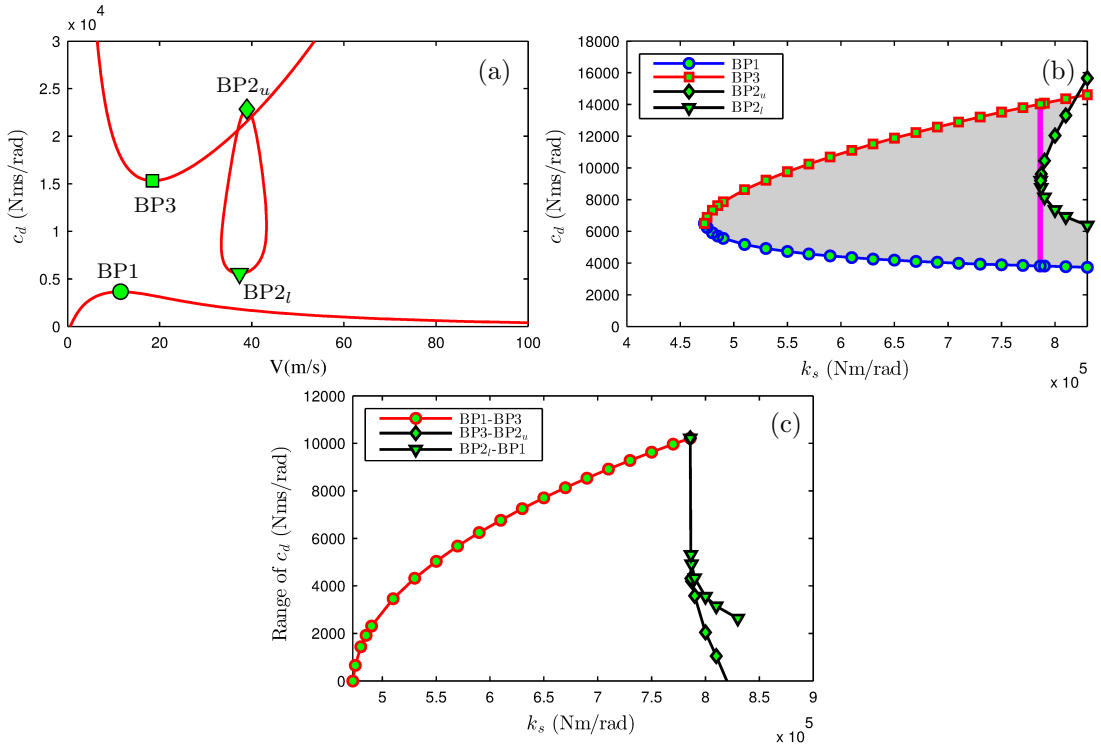

Figure 10: (a) The definitions of four boundary points in two-parameter bifurcation diagrams in the (V, c_d)-plane, (b) the damping values of four boundary points when varying k_s and no-shimmy region in the (k_s, c_d)-plane, (c) the width in damping of the zero-shimmy region for the variation of k_s.

4. Effects of inerter-based shimmy-suppression devices

The performance improvements obtained by the inerter-based vibration-suppression devices have been identified for many industrial applications, such as [12–18, 20, 40–43]. In this section, two variations on layout L2 that include inerters are considered. The MLG's sensitivity to the parameters of these two inerter-based layouts are investigated and their performance advantages on expanding the zero-shimmy regions are then discussed.

4.1. Two candidate inerter-based shimmy-suppression layouts

Fig. 11 shows two inerter-based shimmy-suppression layouts proposed in this work, labelled LI1 and LI2. The layouts are inspired by work on the vibration suppression of buildings. LI1 is referred as a TVMD-type layout, which includes the inerter in parallel with c_d and k_d of L2. This layout was first proposed by Ikago et al. in [44] and was called the tuned-viscous-mass-damper (TVMD). The original layout excludes k_d; we propose k_d here to function as a centering spring. LI2 is a TID-type layout; the original TID (tuned-inerter-damper) layout was introduced by Lazar et al. in [15]. The spring k_s was not introduced in the original layout but is considered here, again acting as a centering stiffness. Note that for both layouts, we focus on the effects of k_s and b while fixing k_d to the value used for the default shimmy damper, 1.09×10^5 Nm/rad. Note also that the two layouts are equivalent to layout L2 if b is set to zero.

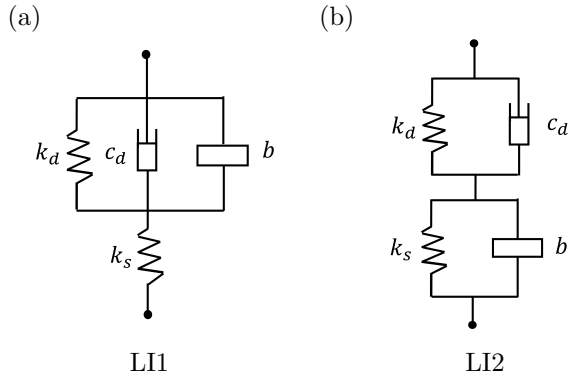

Figure 11: Two candidate inerter-based device layouts, (a) TVMD-type LI1, (b) TID-type LI2.

4.2. Effects of layout LI1

Fig. 12 shows two-parameter bifurcation diagrams for the layout LI1 for several representative values of k_s when fixing b to different values in the range of $b \in [20, 150]$ Nms^2/rad. Note that $b = 0$ result is equivalent to the L2 bifurcation plots of Fig. 9. Several qualitative changes in the appearance of the δ-shimmy regions are observed here. When the inertance b is relatively small such as $b = 20$ Nms^2/rad, changing k_s produces a similar effect to that observed for L2 ($b = 0$). Hence, the width of the zero-shimmy region reaches its maximum just before the δ-shimmy occurs. When b is increased to 30 Nms^2/rad, the first qualitative change is observed – the δ-shimmy curve appears as a narrow-strip below the boundary point BP1 (recall the points BP1–BP4 from Fig. 10(a)) and moves upwards for larger k_s. Consequently, for $b = 30$ Nms^2/rad, the zero-shimmy region is bounded by two points BP1 and BP3 and is maximised just before the upper boundary of the δ-shimmy region BP2$_u$ exceeds BP1. Increasing b to 70 Nms^2/rad produces a similar variation as that seen for $b = 30$ Nms^2/rad case but now the shape of the δ-shimmy region when it appears is a small circle. When b equals 100 Nms^2/rad, the upper boundary of the δ-shimmy region appears higher than BP1. Similar variation trends of the δ-shimmy region are observed for $b = 130$ and 150 Nms^2/rad. Note that for the $b \in [70, 150]$ Nms^2/rad cases, an additional (third) ψ-shimmy dominated region is observed, as illustrated in Figs. 12(c)–(f). However, as this region is much lower than the point BP1 vertically in the (V, c_d)-plane, it will not affect the zero-shimmy region. It can be seen that a higher b or k_s will give rise to a higher third ψ-shimmy region. For $b = 130$ Nms^2/rad, the upper boundary of the third ψ-shimmy region is lower than BP1 when the δ-shimmy

occurs. Here the widest zero-shimmy region is still determined by the two points BP1 and BP3. In contrast, for $b = 150$ Nms^2/rad, the upper boundary of the third ψ-shimmy region grows higher than BP1 before the appearance of the δ-shimmy region. Therefore in this situation, the zero-shimmy region is determined by BP3 and the upper boundary of the third ψ-shimmy region, and reaches the maximum just before the δ-shimmy emerges.

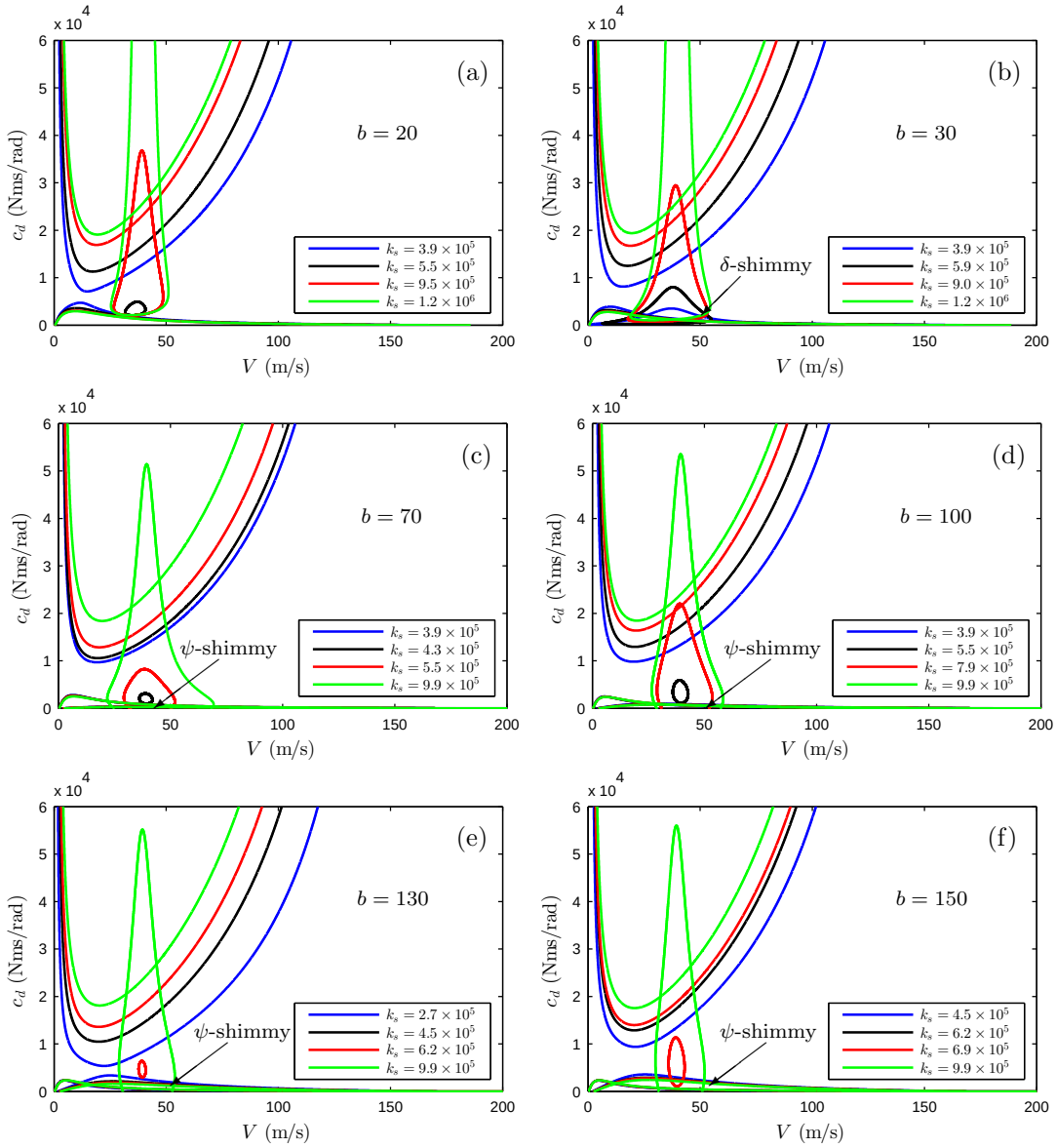

Figure 12: Two-parameter bifurcation diagrams in the (V, c_d)-plane for varying the stiffness k_s (Nm/rad) and b (Nms^2/rad) of LI1. (For interpretation of the references to color in this figure, the reader is referred to the web version of this paper.)

The boundary points in the (V, c_d)-plane are plotted in Figs. 13(a1) and (a2) as k_s and b vary. The zero-shimmy regions are shaded in grey and the vertical lines indicate the maximum width in damping of the zero-shimmy region occurs. In contrast to the results for the layout L2, the lower bounds of the grey areas are not just dependent on BP1 and the maximum width in damping of the zero-shimmy region is not always determined by the appearance of the δ-shimmy. The variation of this width with respect to b (vertical lines in Figs. 13(a1) and (a2)) is plotted in Fig. 13(b). It can be observed that when $b = 140$ Nms^2/rad and $k_s = 6.38 \times 10^5$ Nm/rad, the width of the zero-shimmy region is maximised to 1.12×10^4 Nms/rad ($13561.6 - 2319.1$), with a maximal 9.8% improvement over that with L2 (1.02×10^4 Nms/rad). One notable benefit of the LI1 layout over L2 is that the lower bound of this region, 2319.1 Nms/rad, is significantly smaller than that of L2, 3813.7 Nms/rad. This is potentially beneficial from a manufacturing perspective.

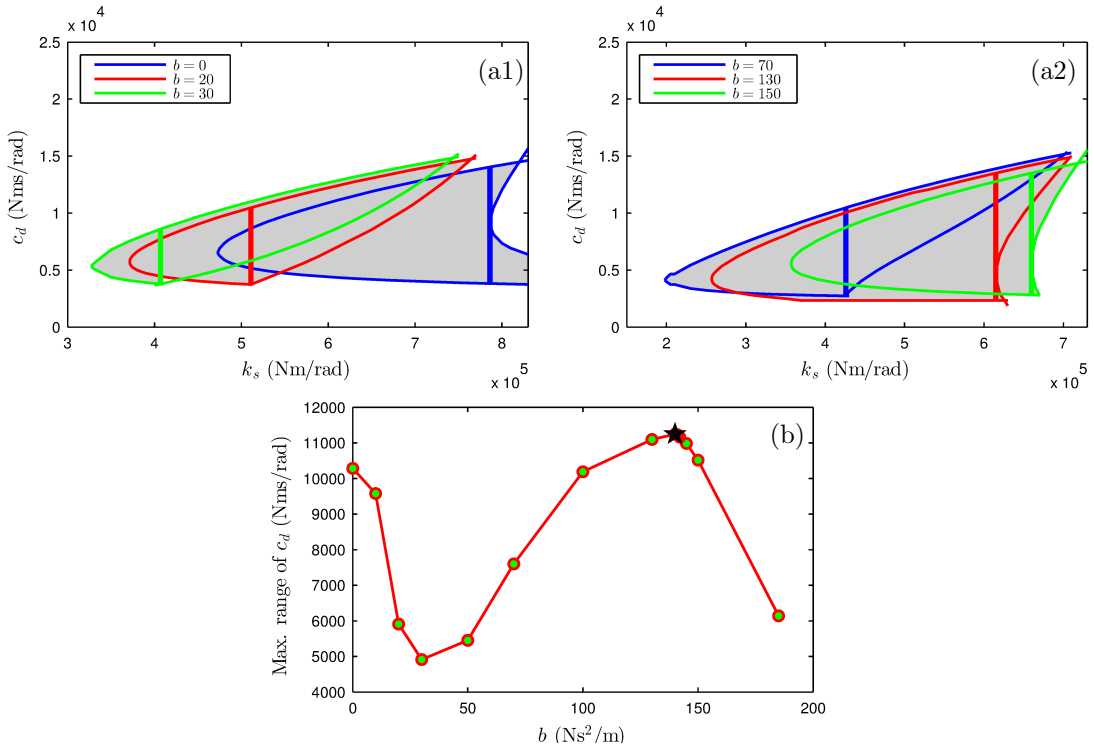

Figure 13: (a) The damping values of boundary points when varying k_s (Nm/rad) and b (Nms^2/rad) of LI1, (b) the maximum width in damping of the zero-shimmy region for the variation of b. (For interpretation of the references to color in this figure, the reader is referred to the web version of this paper.)

4.3. Effects of layout LI2

The same approach is now taken to investigate the influence of layout LI2. Fixing b of LI2 to the specific values, 50 and 100 Nms^2/rad, and then varying k_s, the variations of the bifurcation diagrams in the (V, c_d)-plane are obtained and shown in Fig. 14. The zero-shimmy parameter regions are plotted in the (k_s, c_d)-plane in Fig. 15(a). As for the $b = 0$ case (layout L2), when $b = 50$ Nms^2/rad the maximum width in damping of the zero-shimmy region arises just before the

occurrence of δ-shimmy. If b is increased further, such as to 100 Nms^2/rad, a relatively small k_s will result in a δ-shimmy as shown in Fig. 14(b1). This changes rapidly with the variation of k_s and disappears if k_s is allowed to increase sufficiently. The zero-shimmy region is affected by this δ-shimmy. Hence, as illustrated by the zero-shimmy areas bounded by the magenta and black lines of Fig. 15(a), the left boundaries are not formed by smooth curves. A further increased k_s leads to the appearance of another δ-shimmy region. It can be seen that the width in damping of the zero-shimmy region reaches its maximum value just before this δ-shimmy arises. As with in Fig. 13(b), Fig. 15(b) gives the width in damping of the widest zero-shimmy region of Fig. 15(a) for each b. It can be calculated that the maximum width in damping of the zero-shimmy region increases with b, however, a much larger k_s is required to obtain this maximum value. When comparing with the layout LI1, this growth trend ends with $b = 140$ Nms^2/rad and gives the maximum width in damping as 1.91×10^4 Nms/rad. This width provides a 87.2% improvement over that of L2. It should be noted that this improvement is determined by achievable values of b and k_s which in turn are likely to result in the shimmy-suppression device having a feasible size and weight.

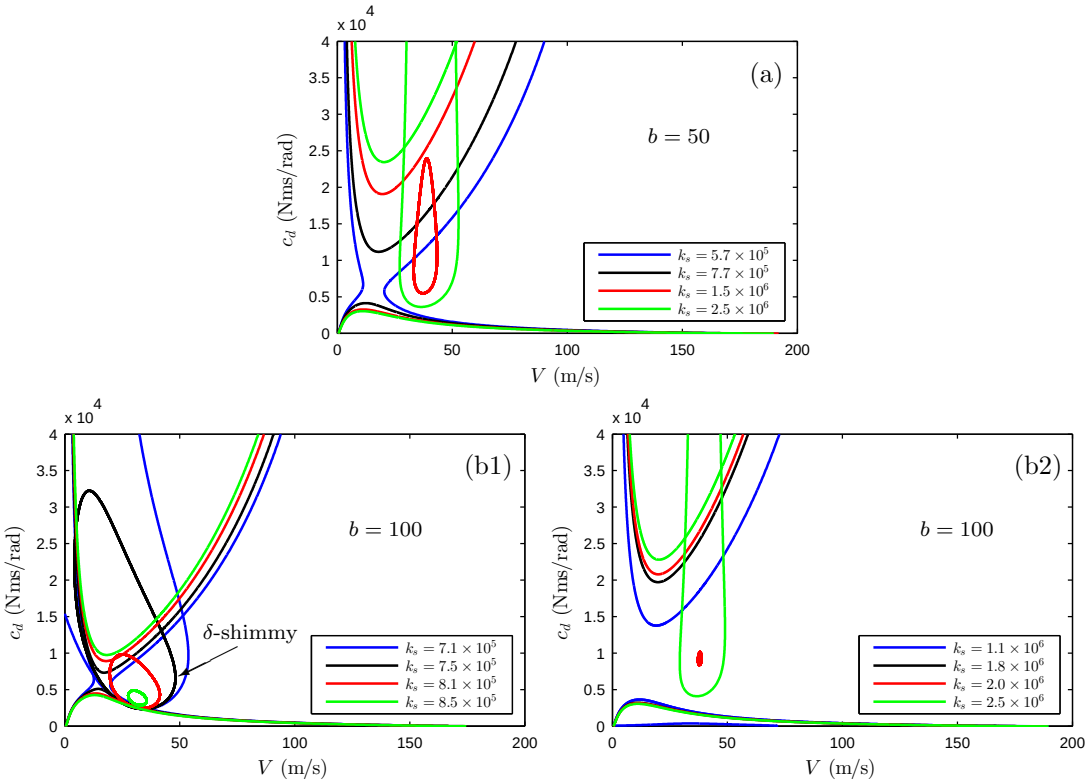

Figure 14: Two-parameter bifurcation diagrams in the (V, c_d)-plane for varying the stiffness k_s (Nm/rad) and b (Nms^2/rad) of LI2. (For interpretation of the references to color in this figure, the reader is referred to the web version of this paper.)

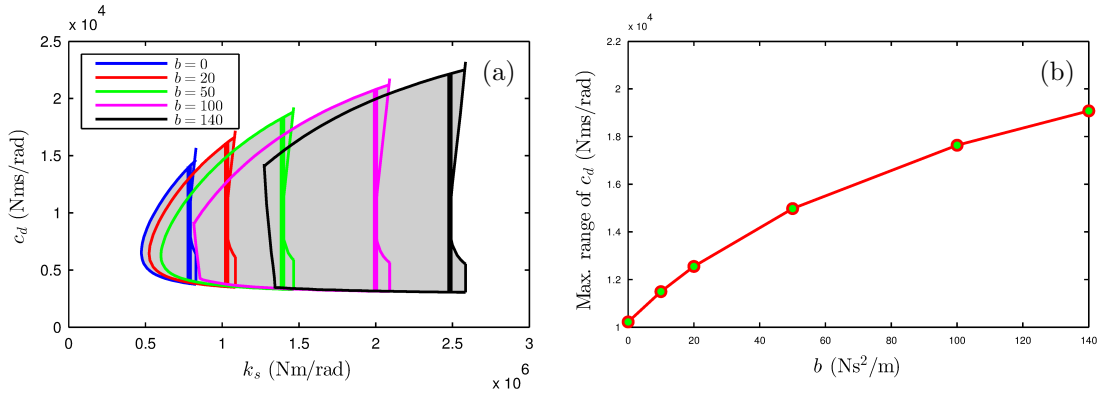

Figure 15: (a) The damping values of four boundary points when varying k_s (Nm/rad) and b (Nms^2/rad) of LI2, (b) the maximum width in damping of the zero-shimmy region for the variation of b. (For interpretation of the references to color in this figure, the reader is referred to the web version of this paper.)

5. Conclusions

This paper investigates the effects of several shimmy-suppression devices on a MLG system and proposes a method of selecting the device parameter values to prevent shimmy for any forward speed within the operating region. The forward velocity V and the device damping c_d are used as continuation parameters to obtain two-dimensional bifurcation diagrams. It is found that, to ensure the MLG is free of shimmy instability for any forward velocity over the considered range, the damping of the conventional shimmy damper (L1) needs to be designed within a narrow range of values and hence a tight tolerance. This device damping range is defined as the width in damping of the zero-shimmy region and needs to be enlarged to provide a larger parametric operating range for the damping device. By adding an additional spring k_s in series with the shimmy-damper layout, a spring-damper layout (L2) is proposed. The effective torsional stiffness of the system is altered, resulting in an enlarged zero-shimmy region. The maximum width in damping of this zero-shimmy region is about 38 times that obtained by the shimmy damper. Consequently, two inerter-combined layouts LI1 and LI2 are proposed. It is found that for LI1 a maximal 9.8% improvement over L2 can be obtained. One notable benefit of the LI1 layout over L2 is that the lower bound of this maximum zero-shimmy region is significantly smaller than that of L2. For LI2, the maximum width in damping of the zero-shimmy region increases significantly with growing b and k_s.

Acknowledgments

The authors would like to acknowledge the support of the EPSRC and the China Scholarship Council: Simon Neild is supported by an EPSRC fellowship EP/K005375/1 and Yuan Li is supported by a China Scholarship Council studentship.

Appendix: equation of motion coefficients

The coefficients N^b_{aa} for the equations of motion are given as follows. For Eq. (32),

$$
\begin{aligned}
N^\delta_{11} &= J^b_{D\xi\xi} + (J^b_{D\xi\xi} - J^b_{D\eta\eta})\cos^2\psi + m_D L_D^2\cos^2\delta,\\
N^\delta_{12} &= m_D l_D\cos\phi\sin\delta, \quad N^\delta_{21} = L_D^2(1-2m_D)\cos\delta\sin\delta,\\
N^\delta_{22} &= -2(J^b_{D\xi\xi} - J^b_{D\eta\eta})\cos\psi\sin\psi, \quad N^\delta_3 = c_\delta, \quad N^\delta_4 = k_\delta,\\
N^\delta_{5i} &= N^\delta_{5i1}(-e - R_i\sin\phi) + N^\delta_{5i2}(l_\delta + R_i\cos\phi) \mp \frac{1}{2}aN^\delta_{5i3} + C_{ki}\sin\phi,\\
N^\delta_6 &= l_D m_D g\sin\delta\cos\phi,
\end{aligned}
$$

where $i = L/R$ and

$$
\begin{aligned}
N^\delta_{5i1} &= \Lambda_i\sin\psi(\sin\phi\cos\delta\sin\theta + \sin\delta\cos\theta) + \cos\phi\cos\delta\sin\psi,\\
N^\delta_{5i2} &= \Lambda_i(-\sin\phi\sin\delta\sin\theta + \cos\delta\cos\theta) - \cos\phi\sin\delta,\\
N^\delta_{5i3} &= -\Lambda_i\cos\psi(\sin\phi\cos\delta\sin\theta + \sin\delta\cos\theta) - \cos\delta\cos\psi\cos\phi.
\end{aligned}
$$

For Eq. (33),

$$
\begin{aligned}
N^\psi_1 &= J^b_{D\zeta\zeta}, \quad N^\psi_{21} = (J^b_{D\xi\xi} - J^b_{D\eta\eta})\cos\psi\sin\phi, \quad N^\psi_3 = c_\psi,\\
N^\psi_{5i} &= N^\psi_{5i1}(-e - R_i\sin\phi) + N^\psi_{5i2}(l_\delta + R_i\cos\phi) \mp \frac{1}{2}aN^\psi_{5i3} - C_{ki}\cos\phi\cos(\delta),
\end{aligned}
$$

where $i = L/R$ and

$$
\begin{aligned}
N^\psi_{5i1} &= \Lambda_i\sin\theta(\sin\phi\sin\delta\cos\psi - \sin\psi\cos\phi) + \cos\phi\sin\delta\cos\psi + \sin\phi\sin\psi,\\
N^\psi_{5i2} &= -\Lambda_i\cos\phi\cos\delta\cos\theta,\\
N^{psi}_{5i3} &= -\Lambda_i(\cos\delta\sin\psi\cos\theta - \sin\theta(\cos\phi\cos\psi + \sin\phi\sin\delta\sin\psi)) + \sin\phi\cos\psi - \cos\phi\sin\delta\sin\psi.
\end{aligned}
$$

For Eq. (34),

$$
N^z_{11} = m_D, \quad N^z_{12} = m_D l_D\cos\phi sin\delta, \quad N^z_{21} = m_D l_D\cos\phi\cos\delta.
$$

References

[1] I. J. M. Besselink, Shimmy of aircraft main landing gears, Ph.D. thesis, TU Delft, Delft University of Technology (2000).

[2] W. Krüger, I. Besselink, D. Cowling, D. Doan, W. Kortüm, W. Krabacher, Aircraft landing gear dynamics: simulation and control, Vehicle System Dynamics 28 (2-3) (1997) 119–158.

[3] H. Hitch, Aircraft ground dynamics, Vehicle System Dynamics 10 (4-5) (1981) 319–332.

[4] D. J. Jones, R. A. Evans, Compact shimmy damper for aircraft landing gear, US Patent App. 13/166,424 (Jan. 26 2012).

[5] N. K. Sura, Lateral response of nonlinear nose wheel landing gear models with torsional free-play, Journal of aircraft 44 (6) (2007) 1991–1997.

[6] G. Pouly, T. H. Huynh, J. P. Lauffenburger, M. Basset, Indirect fuzzy adaptive control for active shimmy damping, IFAC Proceedings Volumes 41 (2) (2008) 15058–15063.

[7] E. Atabay, I. Ozkol, Application of a magnetorheological damper modeled using the current–dependent bouc–wen model for shimmy suppression in a torsional nose landing gear with and without freeplay, Journal of Vibration and Control 20 (11) (2014) 1622–1644.

[8] H. Tourajizadeh, S. Zare, Robust and optimal control of shimmy vibration in aircraft nose landing gear, Aerospace Science and Technology 50 (2016) 1–14.

[9] R. Van der Valk, H. Pacejka, An analysis of a civil aircraft main gear shimmy failure, Vehicle system dynamics 22 (2) (1993) 97–121.

[10] C. Arreaza, K. Behdinan, J. W. Zu, Linear stability analysis and dynamic response of shimmy dampers for main landing gears, Journal of Applied Mechanics 83 (8) (2016) 081002.

[11] M. C. Smith, Synthesis of mechanical networks: the inerter, IEEE Transactions on Automatic Control 47 (10) (2002) 1648–1662.

[12] M. C. Smith, F. C. Wang, Performance benefits in passive vehicle suspensions employing inerters, Vehicle System Dynamics 42 (4) (2004) 235–257.

[13] Y. Shen, L. Chen, X. Yang, D. Shi, J. Yang, Improved design of dynamic vibration absorber by using the inerter and its application in vehicle suspension, Journal of Sound and Vibration 361 (2016) 148–158.

[14] J. Z. Jiang, M. C. Smith, N. E. Houghton, Experimental testing and modelling of a mechanical steering compensator, in: Proceeding of the 3rd Int. Symp. on Communications, Control Signal Processing (ISCCSP), 2007, pp. 249–254.

[15] I. Lazar, S. A. Neild, D. Wagg, Using an inerter-based device for structural vibration suppression, Earthquake Engineering & Structural Dynamics 43 (8) (2014) 1129–1147.

[16] S. Y. Zhang, J. Z. Jiang, S. A. Neild, Optimal configurations for a linear vibration suppression device in a multi-storey building (2016). doi:10.1002/stc.1887.

[17] J. Z. Jiang, A. Z. Matamoros-Sanchez, R. M. Goodall, M. C. Smith, Passive suspensions incorporating inerters for railway vehicles, Vehicle System Dynamics 50 (sup1) (2012) 263–276.

[18] J. Z. Jiang, A. Z. Matamoros-Sanchez, A. Zolotas, R. M. Goodall, M. C. Smith, Passive suspensions for ride quality improvement of two-axle railway vehicles, Proceedings of the Institution of Mechanical Engineers, Part F: Journal of Rail and Rapid Transit 229 (3) (2015) 315–329.

[19] D. Xin, L. Yuance, Z. C. Michael, Application of inerter to aircraft landing gear suspension, in: Proceedings of the 34th Chinese Control Conference (CCC), IEEE, 2015, pp. 2066–2071.

[20] Y. Li, J. Z. Jiang, S. A. Neild, Inerter-based configurations for main landing gear shimmy suppression (2016). doi:10.2514/1.C033964.

[21] L. Segel, Force and moment response of pneumatic tires to lateral motion inputs, Journal of Engineering for Industry 88 (1) (1966) 37–44.

[22] B. Von Schlippe, R. Dietrich, Shimmying of a pneumatic wheel, Lilienthal-Gesellschaft für Luftfahrtforschung, Bericht 140 (1941) 125–160.

[23] G. Somieski, Shimmy analysis of a simple aircraft nose landing gear model using different mathematical methods, Aerospace Science and Technology 1 (8) (1997) 545–555.

[24] M. Goman, G. Zagainov, A. Khramtsovsky, Application of bifurcation methods to nonlinear flight dynamics problems, Progress in Aerospace Sciences 33 (9) (1997) 539–586.

[25] P. Thota, B. Krauskopf, M. Lowenberg, Shimmy in a nonlinear model of an aircraft nose landing gear with non-zero rake angle, in: Proceedings of the 6th European Mechanics Society Nonlinear Dynamics Conference, European Mechanics Society, 2008.

[26] P. Thota, B. Krauskopf, M. Lowenberg, Interaction of torsion and lateral bending in aircraft nose landing gear shimmy, Nonlinear Dynamics 57 (3) (2009) 455–467.

[27] C. Padmanabhan, R. Singh, Analysis of periodically excited non-linear systems by a parametric continuation technique, Journal of Sound and Vibration 184 (1) (1995) 35–58.

[28] C. Howcroft, B. Krauskopf, M. H. Lowenberg, S. A. Neild, Influence of variable side-stay geometry on the shimmy dynamics of an aircraft dual-wheel main landing gear, SIAM Journal on Applied Dynamical Systems 12 (3) (2013) 1181–1209.

[29] N. Terkovics, S. A. Neild, M. Lowenberg, B. Krauskopf, Bifurcation analysis of a coupled nose-landing-gear–fuselage system, Journal of Aircraft 51 (1) (2014) 259–272.

[30] P. Eret, J. Kennedy, G. J. Bennett, Effect of noise reducing components on nose landing gear stability for a mid-size aircraft coupled with vortex shedding and freeplay, Journal of Sound and Vibration 354 (2015) 91–103.

[31] J. T. Gordon, H. E. Merchant, An asymptotic method for predicting amplitudes of nonlinear wheel shimmy, Journal of Aircraft 15 (3) (1978) 155–159.

[32] J. Zhou, L. Zhang, Incremental harmonic balance method for predicting amplitudes of a multi-dof non-linear wheel shimmy system with combined coulomb and quadratic damping, Journal of Sound and Vibration 279 (1) (2005) 403–416.

[33] E. Doedel, H. B. Keller, J. P. Kernevez, Numerical analysis and control of bifurcation problems (i): bifurcation in finite dimensions, International journal of bifurcation and chaos 1 (03) (1991) 493–520.

[34] E. Coetzee, B. Krauskopf, M. Lowenberg, The dynamical systems toolbox: Integrating auto into matlab, in: Proceedings of the 16th US National Congress of Theoretical and Applied Mechanics, 2010.

[35] R. H. Daughterty, A study of the mechanical properties of modern radial aircraft tires, Citeseer, 2003.

[36] D. Takács, G. Stépán, Experiments on quasiperiodic wheel shimmy, Journal of Computational and Nonlinear Dynamics 4 (3) (2009) 031007.

[37] D. Takács, Dynamics of towed wheels: nonlinear theory and experiments, Ph.D. thesis (2010).

[38] Y. A. Kuznetsov, Elements of applied bifurcation theory, Vol. 112, Springer Science & Business Media, 2013.

[39] S. Sharma, E. B. Coetzee, M. H. Lowenberg, S. A. Neild, B. Krauskopf, Numerical continuation and bifurcation analysis in aircraft design: an industrial perspective, Phil. Trans. R. Soc. A 373 (2051) (2015) 20140406.

[40] Y. Hu, M. Z. Chen, Z. Shu, Passive vehicle suspensions employing inerters with multiple performance requirements, Journal of Sound and Vibration 333 (8) (2014) 2212–2225.

[41] S. Evangelou, D. J. Limebeer, R. S. Sharp, M. C. Smith, An H_∞ Loop-Shaping Approach to Steering Control for High-Performance Motorcycles, Vol. 329 of Lecture Notes in Control and Information Sciences, Springer, 2006.

[42] F. C. Wang, C. W. Chen, M. K. Liao, M. F. Hong, Performance analyses of building suspension control with inerters, in: Proceedings of the 46th IEEE Conference on Decision and Control, IEEE, 2007, pp. 3786–3791.

[43] F. C. Wang, M. K. Liao, B. H. Liao, W. J. Su, H. A. Chan, The performance improvements of train suspension systems with mechanical networks employing inerters, Vehicle System Dynamics 47 (7) (2009) 805–830.

[44] K. Ikago, K. Saito, N. Inoue, Seismic control of single-degree-of-freedom structure using tuned viscous mass damper, Earthquake Engineering & Structural Dynamics 41 (3) (2012) 453–474.